water

MDPI

Article

Vortex Impeller-Based Aeration of Groundwater

Maarten V. van de Griend [1,2], Francis Warrener [1,3], Meike van den Akker [1], Yanru Song [1], Elmar C. Fuchs [1,4,*], Willibald Loiskandl [2] and Luewton L. F. Agostinho [1,5]

1 Wetsus, European Centre of Excellence for Sustainable Water Technology, 8911 MA Leeuwarden, The Netherlands; maarten.vandegriend@wetsus.nl (M.V.v.d.G.); franciswarrener@hotmail.com (F.W.); meike.akker@gmail.com (M.v.d.A.); yanru_song@outlook.com (Y.S.); luewton.lemos@wetsus.nl (L.L.F.A.)
2 Institute of Soil Physics and Rural Water Management, University of Natural Resources and Life Sciences, 1190 Vienna, Austria; willibald.loiskandl@boku.ac.at
3 DESA (Departamento de Engenharia Sanitária e Ambiental), Universidade Federal de Minas Gerais, 31270-901 Belo Horizonte, Brazil
4 Optical Sciences Group, Faculty of Science and Technology (TNW), University of Twente, 7522 NB Enschede, The Netherlands
5 Water Technology Research Group, NHL Stenden University of Applied Sciences, 8917 DD Leeuwarden, The Netherlands
* Correspondence: elmar.fuchs@wetsus.nl

Abstract: Iron oxidation and removal from groundwater is a necessary and costly process in drinking water production. In most cases, iron removal is done via aeration, succeeded by precipitation. Most systems for aeration are based on increasing the interfacial area via injecting air in the system or spraying. Both methods have disadvantages, like clogging and formation of aerosols. In this study, a new vortex-based flow-through reactor consisting of a cylindrical tank with an impeller located at the bottom was studied regarding its aeration and iron oxidation capabilities in groundwater. During the aeration experiments, the flow rate, impeller rotation and aerated volume were varied. A nondimensional constant α was proposed to relate the system's physical characteristics and its aeration capabilities, expressed in dissolved oxygen and system volumetric mass transfer coefficient (K_La). Three distinct operational regimes were defined: formation, complete and bubble regime. These regimes showed very specific characteristics regarding the air–water interface structure and the area to volume ratio, resulting in different aeration capabilities and iron oxidation efficiency values. The system presented K_La values similar to commercially available aeration systems, especially inside the bubble regime. By using dimensionless coefficients, the presented analysis provided the basis for the design of continuous impeller aeration and oxidation systems of arbitrary size.

Keywords: aeration; iron oxidation; impeller; vortex; groundwater treatment

Citation: van de Griend, M.V.; Warrener, F.; van den Akker, M.; Song, Y.; Fuchs, E.C.; Loiskandl, W.; Agostinho, L.L.F. Vortex Impeller-Based Aeration of Groundwater. *Water* **2022**, *14*, 795. https://doi.org/10.3390/w14050795

Academic Editor: Domenico Cicchella

Received: 31 January 2022
Accepted: 1 March 2022
Published: 3 March 2022

1. Introduction

Aeration is a commonly used and an important step applied in water and wastewater treatment processes [1,2]. It is a technique in which air and water are brought into close contact, normally with the objective of increasing the dissolved oxygen content in the water body in order to provide, e.g., oxidation of dissolved metals, volatile organic chemicals [3] or maintenance of biota equilibria in open waters. It can also be used, inversely, to decrease the concentration of a specific gas in the liquid phase (in this case, the process is called stripping).

In order to achieve aeration, air must be transported through the gas-liquid interface into the liquid. The process can be carried out with different methods, e.g., diffusion aerators, submerged turbines, jet diffusers, cascades, etc. Diffusion aerators inject gas under pressure into the liquid phase [4]. Fine pore diffusers are an example of such aerators. Due to their high efficiency and low energy consumption, these diffusers are a primary

option for many applications. Another example of commonly used systems are submerged turbines, or so-called machine aerators. In these systems, the liquid is aerated using a submerged rotating turbine or impeller. This technique was developed to solve the clogging problems normally faced when using diffusion aerators.

Aeration is one of the most energy intensive steps in water treatment. Due to this fact, the improvement of such systems is of great interest for the industry [5]. In this work, we presented a study regarding the performance of a novel impeller-based aeration system providing high aeration capabilities and reduced formation of aerosols (reduced splashing) in a compact flow-through setup. The formation of aerosols is an undesirable aspect of water treatment processes as the suspended droplets can be a vector for inhalation of unwanted compounds by operators. Additionally, the performance of the system was tested in terms of its capability to oxidize Fe^{2+}. These characteristics marked the system as a promising technique for drinking water—and especially groundwater—treatment, as for the latter, iron removal is often a necessary step.

Aside from groundwater, aeration is also an important step in wastewater treatment. Some wastewater treatment plants use a combination of diffusers and machine aerators [4]. Aeration comprises a good fraction of total energy costs. Rosso et al. [6] reported that the energy consumption of currently available aeration systems ranged between 45% and 75% of the total energy consumption in wastewater treatment plants. Although not the focus of this work, the abovementioned issues could potentially be addressed with this proposed system.

1.1. Iron Oxidation

Iron is present in groundwater due to percolation of rain through sand, rocks and other materials [7]. In general, the iron concentration found in groundwater does not affect human health, though it can have undesirable effects such as discoloration, turbidity, bad taste, staining and deposition on solid surfaces, causing problems, especially in the distribution system [8]. Iron occurs mainly in two states: dissolved divalent iron (Fe^{2+}) and trivalent or ferric iron (Fe^{3+}) [7]. Ferric iron is less soluble than divalent iron and can therefore be removed with filtration [9].

A common approach taken to remove undesirable concentrations of dissolved iron from ground water is oxidation via aeration, followed by a filtration step. In this process, the divalent iron loses an electron to the oxygen, creating ferric iron and water (Equation (1)). The ferric iron then reacts with water and precipitates as iron hydroxide, $Fe(OH)_3$ (Equation (2)). The sum of these reactions is given in Equation (3),

$$Fe^{2+} + \frac{1}{4}\,O_2 + H^+ \rightarrow Fe^{3+} + \frac{1}{2}\,H_2O \quad (1)$$

$$Fe^{3+} + 3\,H_2O \rightarrow Fe(OH)_3 \downarrow + 3\,H^+ \quad (2)$$

$$Fe^{2+} + \frac{1}{4}\,O_2 + 2\frac{1}{2}\,H_2O \rightarrow Fe(OH)_3 \downarrow + 2\,H^+ \quad (3)$$

The reaction is pH dependent [8]. At a pH value of about 8, the solubility of $Fe(OH)_3$ is lowest, and the hydroxide (as a solid) can be more easily removed in the filtration step [9]. The necessary oxygen is brought via aeration. A comparison of the efficiency of different ground water iron oxidation systems is given in Table 1.

Table 1. Iron oxidation efficiencies before the liquid enters the filter bed.

Reference	Method	$[Fe^{2+}]$ Inlet/mg/L	pH	Iron Oxidation Efficiency/%
[10]	Diffused aeration	6.10	6.97–7.14	88–95
[3]	Diffused aeration	not stated	6	66–72
[11]	Diffused aeration	0.65	8.39–8.51	14–39
[12]	Spray aeration	0.85	6.4	49
[8]	Cascade aeration	1.8	7.6	70–85

After oxidation, the hydroxide formed can be removed by various methods. Since it resembles a suspended particle, a logical, frequently applied step is sand filtration. Membranes can also be used, but are often avoided, as scaling via iron precipitation can be a big issue in such systems. Depending on environmental and chemical parameters, the iron process can be categorized into three types: homogeneous, heterogeneous and biological [13]. Since for these processes, an aeration step is necessary, by setting the parameters accordingly, the presented impeller aerator could, in principle, be applied for all types of iron oxidation.

1.2. Impeller Based Aeration

Impellers can be used in different mixing processes, such as blending of substances, generating gas–liquid exchange or suspending particles in a fluid medium [14]. Different types of impellers produce distinct flows that can be used for different purposes. The optimum design of a stirred tank depends on the desired process and is achieved by the correct choice of tank and impeller geometry, impeller position in the vessel, rotational speed, type of fluid and inlet–outlet location [15].

Impeller-based aeration systems, also known as stirred tanks, are commonly used for mixing, creating solid suspensions and gas dispersion for industrial, chemical, pharmaceutical and food processes, as well as in industrial and municipal wastewater treatment plants [16]. Regarding the position of the impeller they can be submerged or floating stirrers. Some studies have reported that the use of submerged stirrers, contrary to floating ones, increased system efficiency [17,18].

Impellers can also be described according to the type of flow produced by their rotation. Axial flow impellers primarily move the liquid up and down whereas radial flow impellers primarily move the liquid to the side and back again [18]. The design of an impeller is important for the operation of an aeration system and can also help to reduce running costs [15,19]. Zheng et al. [19] investigated how different impeller designs can influence energy consumption in aeration systems. According to these authors, a fan-shaped turbine performed best in terms of gas dispersion and energy efficiency. When the airflow reaches the central disk, it is guided to the blades on the sides.

The most used approach to characterize the efficiency of an impeller is the volumetric mass transfer coefficient K_La, a parameter that combines the mass transfer coefficient K_L and a, the gas–liquid interface area divided by tank volume. In most cases, the separate experimental determination of K_L and a is a rather complex task. Therefore, the two terms are generally combined [18]. This approach is described in detail in Section 2.2. For a given liquid, the magnitude of K_La mainly depends on the interface area. Prediction and measurement of the volumetric mass transfer coefficient is therefore essential in order to establish the aeration efficiency—and for the design of aeration systems [20].

Additionally, as recently shown by Baeten et al. [21], the height of the tank in a bubble aeration system, i.e., system geometry, can have effects on the aeration efficiency. The authors investigated the effect of the vertical gradient of gas phase composition and the pressure on the total stripping and absorption rate of volatile substances in tall reactors. They showed that the increase in the length of the reactor showed an almost linear correlation to the increase in the stripping rate. This effect could be explained by a longer

residence time of the gas which allowed enhanced gas transport and diffusion. When the K_La doubled, the stripping rate also doubled [21].

A more theoretical approach was taken by Nienow et al. [22], who tried to correlate gas dispersion with operational conditions of Rushton turbine agitators using dimensionless variables. The authors proposed two numbers governing aeration rate: the Froude number (Fr) and the aeration number (Fl_g). The key application of these operational variables was the relation between the impeller diameter, the tank diameter and the gas flow rate [18]. These parameters are crucial for designing and upscaling impeller-based aeration systems. They are shown below in Equations (4) and (5),

$$Fr = \omega^2 D \cdot g^{-1} \quad (4)$$

$$Fl_g = 13 D^5 {D_T}^{-5} Fr^2 \quad (5)$$

where ω (s^{-1}) is the impeller rotation rate, D (m) is the impeller diameter, g (9.81 $m \cdot s^{-2}$) is the gravitational acceleration constant and D_T (m) the tank diameter.

1.3. Vortices

When an impeller is spinning, the angular velocity of the liquid is increased due to the rotating motion of an impeller and the redistribution of vorticity. This effect leads to a deformation of the free surface, normally present in form of a vortex. As the rotation of the impeller increases, the width and the depth of the vortex also increases [17,23,24].

Free surface vortices are used for various engineering and industrial applications [25]. They can be formed during the operation of impeller-based aeration systems [17], and thus are commonly seen in aeration, gas stripping and mixing systems. The vortex flows occur when concentrated air vortices encounter a liquid surface in an open channel. This interaction leads to increased rotation and depression on the liquid–air interface. The structure acquired by the liquid due to this rotation is often related to a whirlpool or a maelstrom.

When a vortex is formed in a liquid, the angular momentum must be conserved. A particle moving towards the intake of a closed system only needs a little vorticity to generate a surface dip at the center. The steady application of energy ensures the formation of a stable vortex with a full air core [25].

2. Materials and Methods

The impeller used in this work is shown in Figures 1 and 2. It was a prototype from the company H2MOTION [26], resembling a hyperbolic frustum with an opening in the center and air outlets at the bottom. In contrast to most other systems, this configuration allowed air to be sucked into the impeller and consequently being expelled at its bottom, provided that the rotational velocity is high enough.

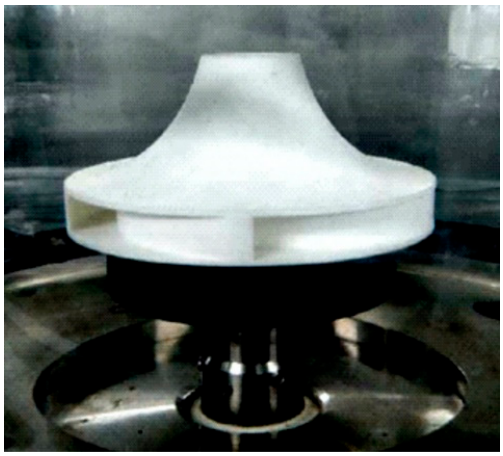

Figure 1. Image of the impeller investigated in this work (Prototype designed by the company H2MOTION [26]).

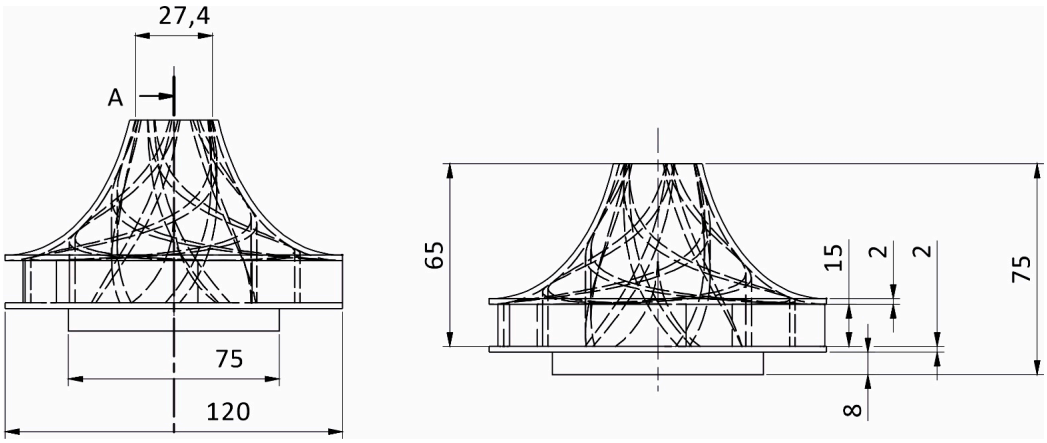

Figure 2. Technical drawing of impeller investigated in this study [26]. The numbers represent the different measures in mm.

The setup used for the experiments conducted for this work is shown in Figure 3. A SAER Electropump M150 was used to pump groundwater from the lab well to the setup's inlet. The groundwater composition was evaluated prior to the experiments. The evaluated parameters and the obtained results are tabulated in Table 2.

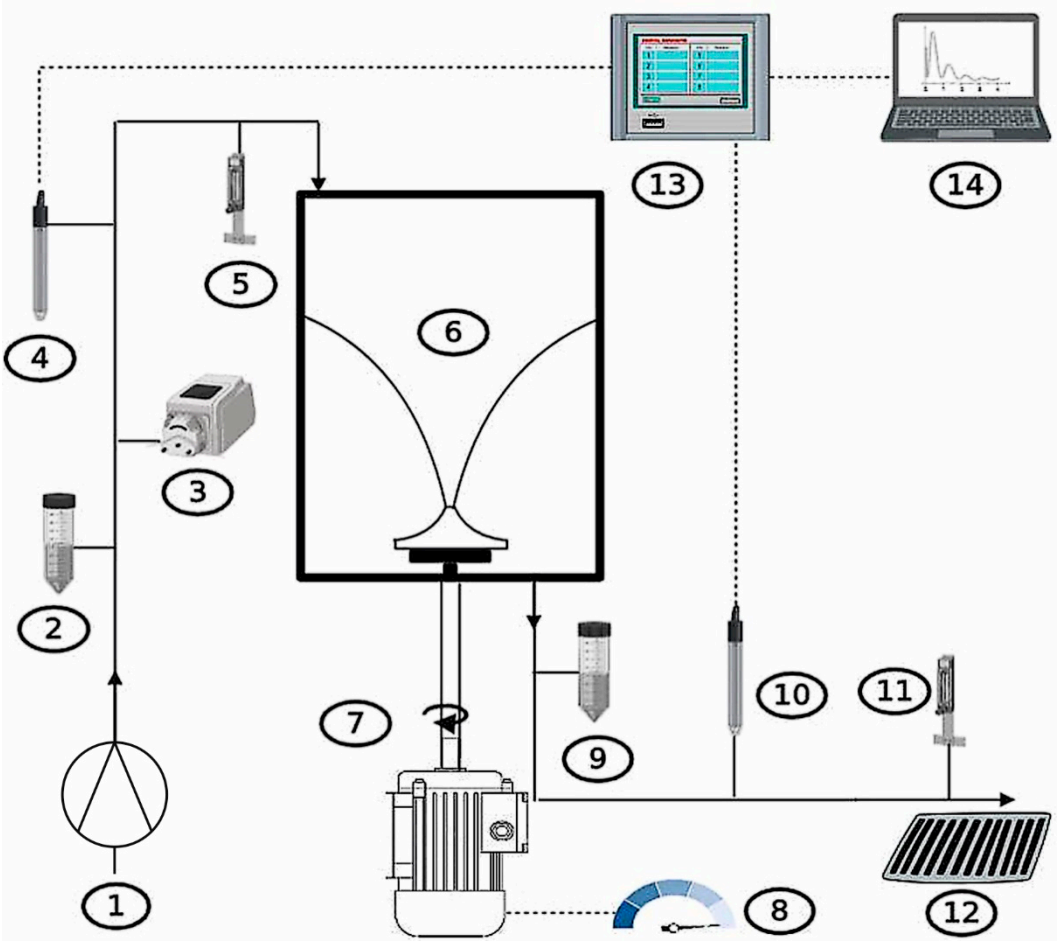

Figure 3. Experimental vortex aeration setup: (1) water pump, (2) inlet sampling point, (3) NaOH dosing pump, (4) inlet Redox, pH and DO sensors, (5) inlet flow meter, (6) vortex aeration tank, (7) engine, (8) rotation control, (9) outlet sampling point, (10) outlet Redox, pH, and DO sensors, (11) outlet flow meter, (12) drain, (13) data logger, (14) computer.

Table 2. Chemical analysis, IC, TC, TOC, pH, redox potential and temperature of the groundwater used in the experiments.

Parameter	Result	Unit	Measuring Device
Chloride	>800	mg L^{-1}	Metrohm 930 compact IC flex
Inorganic Carbon (IC)	114	mg L^{-1}	Shimadzu TOC-L in combination with ASI-L
Total Carbon (TC)	135	mg L^{-1}	Shimadzu TOC-L in combination with ASI-L
Total Organic Carbon (TOC)	20.4	mg L^{-1}	Shimadzu TOC-L in combination with ASI-L
Iron	4.58	mg L^{-1}	Perkin-Elmer ICP OES Optima 5300 DV
Manganese	0.405	mg L^{-1}	Perkin-Elmer ICP OES Optima 5300 DV
Sodium	>400	mg L^{-1}	Perkin-Elmer ICP OES Optima 5300 DV
NH_4^+	3	mg L^{-1}	Metrohm 930 compact IC flex
CH_4	2–5	mg L^{-1}	Varian CP-4900 Micro-GC
H_2S	<0.13	mg L^{-1}	Varian CP-4900 Micro-GC
pH	6.9	-	Endress + Hauser memosens orbisint CPS11D
Dissolved Oxygen (DO)	0.002	mg L^{-1}	PreSens® PSt3 Sensor
Redox Potential	−200	mV	Endress + Hauser memosens orbisint CPS12D
Temperature	13	°C	PT100 thermocouple

In the inlet system, NaOH with a concentration of 0.075 M was dosed using a SIMDOS 10 UFEM 1.10 S2 membrane dosing pump (KNF Ferder B.V., Vleuten, The Netherlands),

in order to adjust the pH. After the NaOH dosing point, the water passed through three T-junctions with pH, Redox potential and a dissolved oxygen (DO) sensor connected. After that, the flow passed through a flow meter (Picomag DMA15-AAABA1, Endress + Hauser AG, Reinach BL, Switzerland) and finally entered the aeration tank.

Before filling the tank, the impeller rotation rate necessary for the experiment was adjusted using the rotor rotation control. The engine used was sufficiently strong to compensate for the friction of the water; thus, the rotation rate decrease when water was added was negligible. The rate was measured using a VOLTCRAFT rotation meter (Conrad Electronics SE, Hirschau, Germany). Then, the rotor was stopped and the tank filling process started. The tank inlet was located at its top part; however, the tubing continued all the way down to the bottom to ensure that there was no extra turbulence that could increase the dissolved oxygen concentration of the feed. The tank was filled to a previously defined water level to allow experiments to be conducted with different volumes (see Table 3). After the tank was filled up to the desired level, the outlet valve was opened. In the drain line, a second set of pH, redox potential and DO sensors allowed us to measure these parameters for the outlet. Finally, before completely exiting the system, the water passed through another flow meter. The inlet and outlet flow meters were used to equalize the flows guaranteeing a constant volume in the aeration tank.

Table 3. Description of the one-pass system experiments.

Height h/m	Rotational Speed ω/rpm	Flow Rate φ/L·min^{-1}
0.3	210; 350; 700; 750; 800; 1000	0.38; 0.8; 1.2; 2.5
0.5	210; 350; 700; 1000	0.8
0.7	210; 350; 750; 1000	1.2

Depending on operational parameters, the system generated three different shapes of the air–water interface, representing three aeration regimes. These were: a formation regime, where the rotation was not yet strong enough for air to enter the impeller; a complete regime, where air has entered the impeller from the top, but has not yet been ejected on the sides; and a bubble regime, where air has been ejected in the form of bubbles (The different regimes are explained in more detail in Section 3.1). In order to better understand the influence of the parameters on these regimes, a series of experiments was done with different aeration volumes (water heights) and impeller rotation rates. The relation between impeller diameter and tank diameter was kept constant at a ratio of 2/5. The temperature changes during the treatment were negligible.

Table 4 lists all sensors used for the experiments. A sampling time of three seconds was attributed to all sensors. Measured data was collected using a data logger (Memograph RSG40, Endress Hauser, Reinach BL, Switzerland). Groundwater samples for measuring Fe^{2+} and Fe^{3+} concentrations were collected both at the inlet and outlet after one hydraulic retention time (HRT, the water volume divided by the feeding flow rate), to ensure comparability of data. The iron analyses were performed using Hach® Lange LCK 320 Iron tests using the 1,10-Phenanthroline method [27].

Table 4. List of sensors used at the inlet and outlet.

Type	Model	Measuring Principle
pH	Endress + Hauser® memosens orbisint CPS11D	Glass Electrode
Redox potential	Endress + Hauser® memosens orbisint CPS12D	Glass Electrode
DO	PreSens® PSt3 Sensor	Optical Fiber Sensor

In order to measure the oxygen transfer capability of the system a total of 32 experiments were performed (see Table 3), varying groundwater flow rate φ, impeller rotation ω and water height h. The objective of these experiments was to relate the final DO concentra-

tion, the K_La, the area to volume ratio, A/V, and the nondimensional coefficient α (defined in Section 2.1) to these three variables.

Additional experiments were conducted to test the iron oxidation performance at different pH conditions. These tests were performed with h = 0.3 m, three different rotation velocities (ω = 350, 750 and 1000 rpm), a flow rate φ = 0.38 L min^{-1} and four different pH values (6.9, 7.3, 7.7, and 8.1). The pH values were chosen according to the work of van Beek et al. [28] to guarantee that oxidation would take place inside the homogenous zone, heterogeneous zone and biological zone, respectively.

2.1. Determination of the K_La Value

It is known that there are different challenges to experimentally define the K_La in an aeration system, mostly caused by the difficulty of precisely determining the interface area. Such challenges make comparisons between different aeration systems rather difficult [20]. Often, more theoretical approaches are proposed to tackle this problem. Among the different methods, the gas out—gas in approach has been described as one of the most reliable [18,29,30]. In this method, the oxygen volumetric transfer rate of the system, dC/dt, is defined as the product between the volumetric mass transfer coefficient K_La and the gas concentration gradient relative to saturation [28], as shown in Equation (6),

$$\mathrm{d}C/\mathrm{d}t = mi_{L-G} = K_L\, a \cdot (C_S - C) \tag{6}$$

where C is the DO concentration in mg·L^{-1} and C_S the DO saturation concentration in mg·L^{-1} at the same temperature.

The mass balance of oxygen in the system can be expressed using

$$\varphi \cdot C_{in}.t + K_L\, a \cdot V \cdot (C_S - C_{out}) \cdot t = \varphi \cdot C_{out} \cdot t \tag{7}$$

where φ is the flow rate in m^3·h^{-1}, C_{in} the DO concentration at the inlet in mg·L^{-1}, V is the volume in m^3, t the time in h and C_{out} the DO concentration at the outlet in mg·L^{-1}. Therefore, K_La can be calculated according to Equation (8),

$$K_La = \varphi\, (C_{out} - C_{in})\, V^{-1}\, (C_S - C_{out})^{-1} \tag{8}$$

In order to relate the aeration number Fl_g [18] with the geometry of the tank, we proposed the nondimensional coefficient α according to Equation (9),

$$\alpha = \log_{10}(Fl_g\left(h \cdot {D_T}^{-1}\right)^{-1}), \tag{9}$$

where Fl_g denotes the aeration number, h the height and D_T the diameter of the tank, respectively. The use of a logarithm was chosen to create values in the operating range that were easy to work with. α was calculated for rotations between 100 and 2000 rpm and for water heights of 0.3, 0.4, 0.5, 0.6 and 0.7 m, that corresponded in volumes of 21, 28, 35, 42 and 49 L, respectively. This coefficient combined the tank geometry, the impeller geometry and the rotation in a single number that could be used to distinguish different vortex regimes and help in aeration system design. When combined with other coefficients like K_La, it facilitates understanding of how the different aeration regimes contribute to the aeration behavior.

2.2. Determination of the Gas/Liquid Interface

In order to determine the relationship between the aeration rate and the size of the diffusive surface (normally expressed as the system area to volume ratio "a"), an image analysis of the interface formed in different regimes was performed. To this end, images of the impeller reactor were taken from a side view using different water column heights (30, 40, 50, 60 and 70 cm) and impeller rotation rates (210, 350 rpm, and every 50 rpm between 550 and 1000 rpm) intervals. The images were taken with a Nikon D7200 and the interfacial

areas generated in each situation were subsequently calculated in the following way: first, the images were preprocessed in Fiji® by edge determination and manual blacking out of areas with larger radii than the visual location of the interface. The scale of the picture was determined from the diameter of the glass vessel (300 mm) as a reference. Next, a program written in Python® determined the location of the interface for every vertical pixel position. For a given pixel row, a threshold of 10% of the maximum pixel value in the row was set and, from both sides, a test was performed to determine when this value was first exceeded. These two pixel positions were then considered to be the instantaneous position of the interface. In the bubble regime, the presence of bubbles blocked the view of the central interface, especially in the bottom part of the reactor. Therefore, only the upper part of the image was considered. Additionally, in this regime, an additional area was present via the interface created by the bubbles emerging from the impeller. This area could not be measured and was not included in the calculations.

Since the interface position fluctuated during the course of the experiments, averaging was performed. It is known that the interface created by an irrotational vortex with constant fluid density forms a hyperboloid, also known as Gabriel's horn [31]. This form corresponds to a shape where the surface drops inversely with the radius squared. The space above the impeller resembled such a flow, since water has low viscosity. Additionally, before flowing through the impeller inlet, no extra vorticity is introduced by boundaries in this region. We fitted the determined interface position, as described above, with a hyperboloid using orthogonal distance regression (ODR) [32]. Errors of this method were calculated and taken into consideration. The area of this hyperboloid was subsequently calculated between the inlet of the impeller and the radius of the reactor. For the bubble regime where the visibility was obstructed, the fit was extrapolated to these boundaries.

2.3. Determination of the Iron Oxidation Efficiency

In order to determine the iron oxidation efficiency of the system, 12 experiments were performed in duplicate. In each experiment, one inlet sample was taken in the beginning and one was taken after one HRT. Airtight sampling points were installed in the inlet and outlet, and the samples were taken with glass syringes. The concentrations of Fe^{2+} and Fe^{3+} were measured in each sample using Hach® Lange LCK 320 Iron tests that used the 1,10-Phenanthroline method [27]. The iron oxidation η_{ox} efficiency of each test was determined using Equation (10),

$$\eta_{ox} = \frac{Fe^{2+}_{IN} - Fe^{2+}_{OUT}}{Fe^{2+}_{IN}} \quad (10)$$

3. Results and Discussion

3.1. Vortex Regimes

Figure 4 shows a series of images of the different regimes obtained during the experiments performed with 30 and 40 cm water level and different rotation rates.

The different regimes can be described as follows:

- Regime (1)*: Formation:* This regime happens at low rotation rates. In this case, the rotation causes the formation of a liquid–air interface, normally seen as a small notch at the air–water interface. Even though the interface is deformed, the vortex is not yet completely established, and the liquid–air interface is not contacting the impeller. α values are low (Figure 4a,d).
- Regime (2): *Complete:* This regime can be established when the rotation rates are increased. The liquid surface makes contact with the impeller and the vortex is fully formed, but air is drawn into the impeller. α values are intermediate (Figure 4b,e,f).
- Regime (3): *Bubble:* Upon further increase of the rotation rate, air is drawn into the impeller and ejected as bubbles in the lower part of the reactor (Figure 4c). This regime could not be obtained for 40 cm column height because the rotor could not provide rotation rates higher than 1100 rpm (Figure 4f still represents the complete

regime, since no bubbles were ejected). In the bubble regime, the highest α values were obtained.

The vortex regime is dependent on the type and speed of the impeller, the dimensions of the aeration tank and the type of liquid. The first two regimes are commonly observed with impellers, whereas the third one is specific for the impeller used in this work. In this study, tests with different rotation rates and water heights were performed in order to determine the onset of each regime for the chosen experimental conditions. The transition between the different regimes was determined using the previously defined nondimensional coefficient α (see Equation (9)). Figure 5 shows a diagram for easy comprehension of the variability of α for the different volumes and regimes.

The transition from regime 1 (formation) to regime 2 (complete) started at α values of ~5.2. The transition from regime 2 to regime 3 (bubble) started at α values of ~6.5. As indicated by the color gradients in Figure 5, the transition between the different regimes was not sharp. Table 5 shows the α values at the onset of the regime transitions for different volumes (represented as water column heights).

Table 5. Critical α values indicating a change of vortex regime for different water heights; the first transition occurring from formation to complete, and the second from complete to bubble regime, respectively. An asterisk (*) means that for the α value shown the bubble regime was not obtained due to limitations of the maximum achievable rotation rate, thus the actual values are higher than indicated.

Height h/m	Volume V/L	α For the Onset of the First Regime Transition	α For the Onset of the Second Regime Transition
0.3	21	5.21	6.91
0.4	28	5.79	7.17
0.5	35	5.87	>6.46 *
0.6	42	5.96	>6.50 *
0.7	49	5.89	>6.65 *

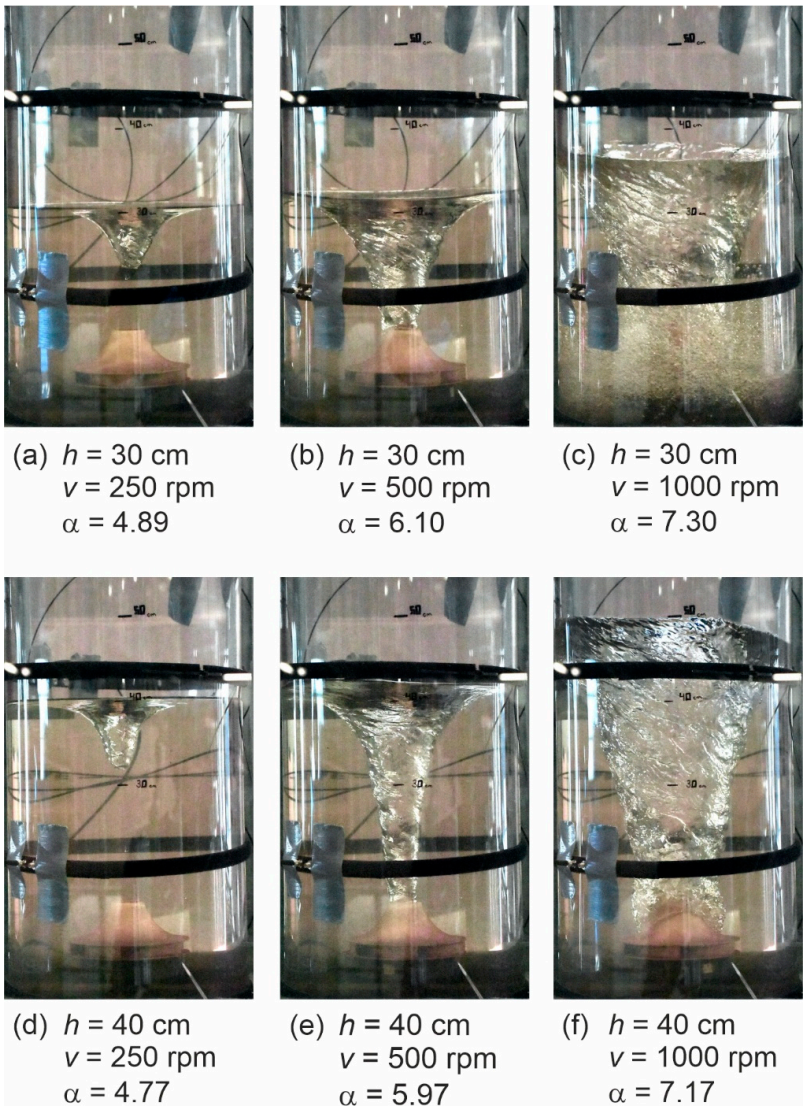

Figure 4. Images of the system for different water levels and impeller rotation rates. For every situation, α is shown. (**a**,**d**) are examples for the formation regime; (**b**,**e**,**f**) for the complete regime, and (**c**) for the bubble regime.

As seen in Figure 5, there was a variation of 0.7 between the minimum and maximum value for the transition from the formation to the complete regime, depending on the experimental combinations for volume and rotation rates. Inside this interval (denoted as 1 . . . 2), especially when close to the lower limit, the authors observed that the interface shape would sometimes be inside one or the other regime, or would even slightly oscillate between the two. The same variation was found for the transition from the complete to the bubble regime (denoted as 2 . . . 3). An interesting behavior was observed for values close to 7.2, with the system sometimes producing bubbles and sometimes not, again blurring the transition line into a transition regime. To facilitate the definition of the aeration systems, we decided to include the two transition regimes into the complete regime, which hence ranged from α = 5.2 to 7.2, while the transition regimes were indicated as part of the complete regime in all following graphs by dotted lines and color gradients. Each regime described above was investigated regarding its physical and chemical properties, including interfacial area to volume ratio, aeration capabilities and iron oxidation efficiency.

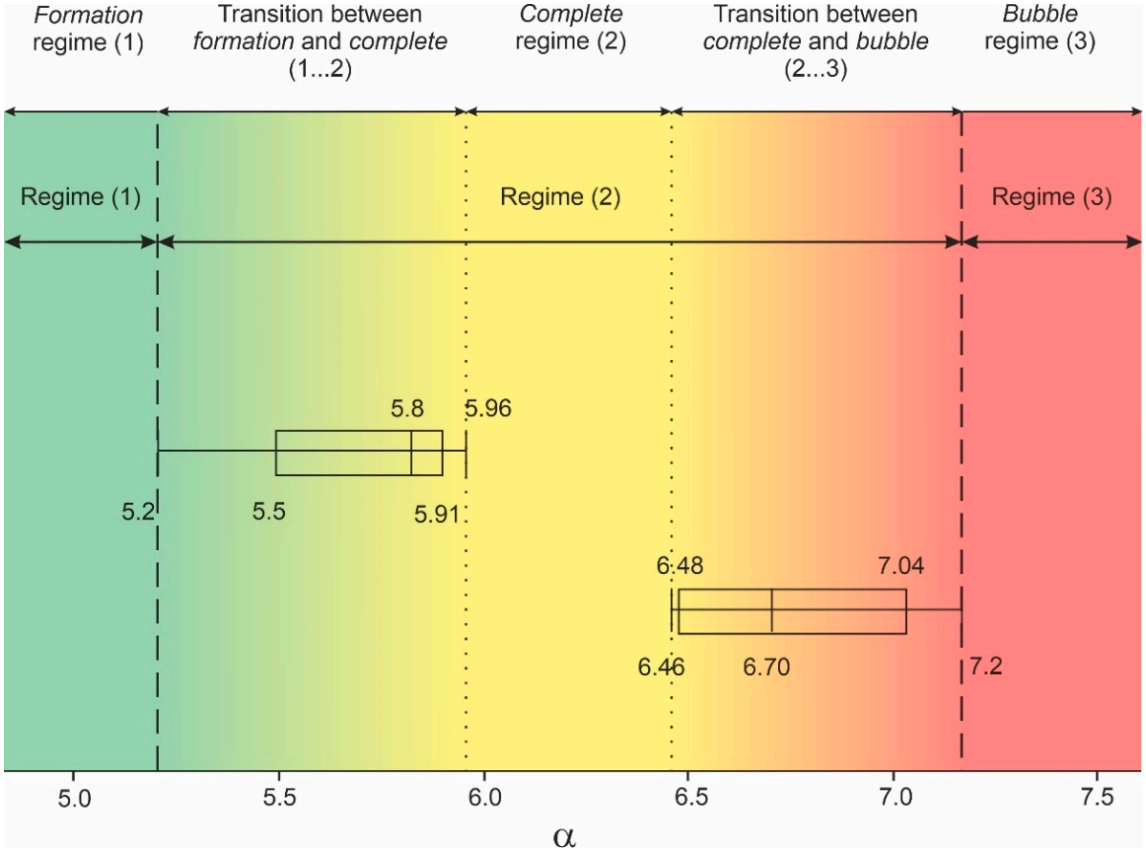

Figure 5. A box plot of the α values indicative of the regimes: (1) formation regime (2) complete regime and (3) *bubble* regime, as well as transition regimes in between them. The dashed lines indicate regime transitions; the dotted lines show the intra-regime transitions within the complete regime.

3.2. Determination of the Gas/Liquid Interfacial Area

The K_La value is a direct function of the mean interfacial area and the liquid volume in aeration systems, as well as the diffusion coefficient K_L. The interfacial area is composed of two parts: The central surface dip extending downwards and outwards, characteristic of a multiphase vortex, and the area of the bubbles created at the impeller outlets. We performed an image analysis on the central interface which resulted in an additional interface to volume (A/V) ratio shown in Figure 6 as a function of α. Here only additional surface area created by the vortex was considered, not the original interfacial area of the liquid at zero rotation. The logarithm of (A/V) and α can be satisfactorily fit with a linear correlation, especially in the *complete* regime. From combining Equations (4), (5) and (9), it can be seen that A/V behaves linearly in ω^4, meaning that the additional area is directly proportional to the fourth power of the rotational velocity.

3.3. Aeration

Figure 7 relates the different vortex regimes to the equilibrium DO concentration. It also presents the lower and upper DO saturation concentrations denoted as $S(T_{max})$ and $S(T_{min})$ for the lowest and the highest water temperature measured during the experiments, calculated from [33].

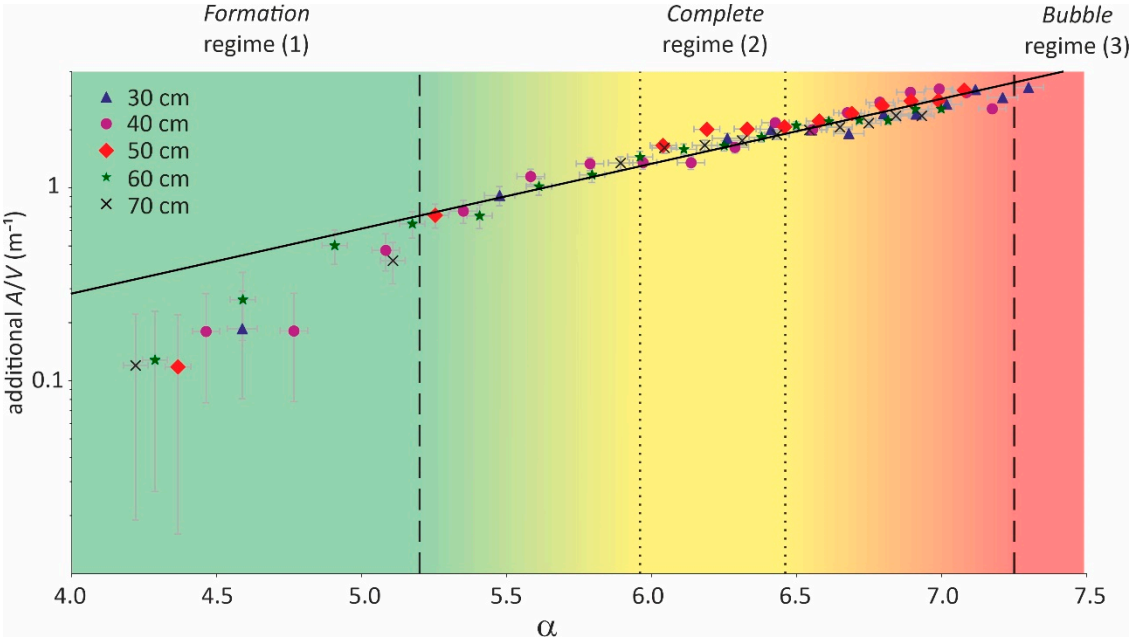

Figure 6. $\log(A/V)$ as a linear function of α. The area considered is only the additional area created by the vortex. A linear regression yields $\log(A/V) = 0.775\alpha - 1.89$. The dashed lines indicate regime transitions; the dotted lines show the intra-regime transitions within the complete regime.

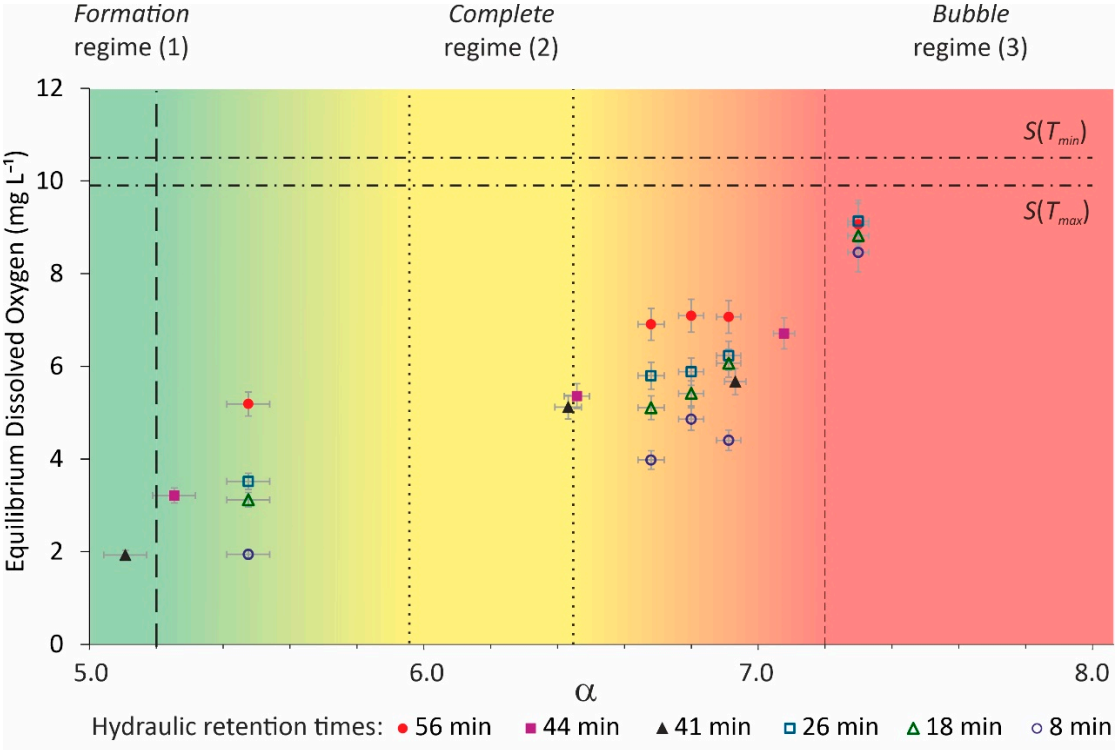

Figure 7. Equilibrium-dissolved oxygen reached for different α values for different hydraulic retention times. Temperature-dependent maximum and minimum saturation concentrations $S(T_{max})$ and $S(T_{min})$ calculated from [33]. The dashed lines indicate regime transitions; the dotted lines show the intra-regime transitions within the complete regime.

DO_{eq} increased with respect to α and seemed to increase more steeply into the bubble regime, when considering the values obtained within the same HRT. This was probably

caused by increase of the interfacial area created by the bubbles in that regime compared to the previous ones. Another interesting aspect was the fact that, inside this regime, the DO_{eq} reached values very close to saturation, even for the smallest HRT (8 min). Thus, long HRTs produced higher DO_{eq} inside the same regime. The difference could be close to twice as much when comparing, for example, the values obtained for HRT = 8 min and HRT = 56 min with α = 6.8. Inside the complete regime (2), the system could provide DO_{eq} values close to the saturation concentration only with an HRT of 56 min.

A plot of K_La against α is shown in Figure 8, showing the rather high values of K_La obtainable with the system investigated, especially in the bubble regime.

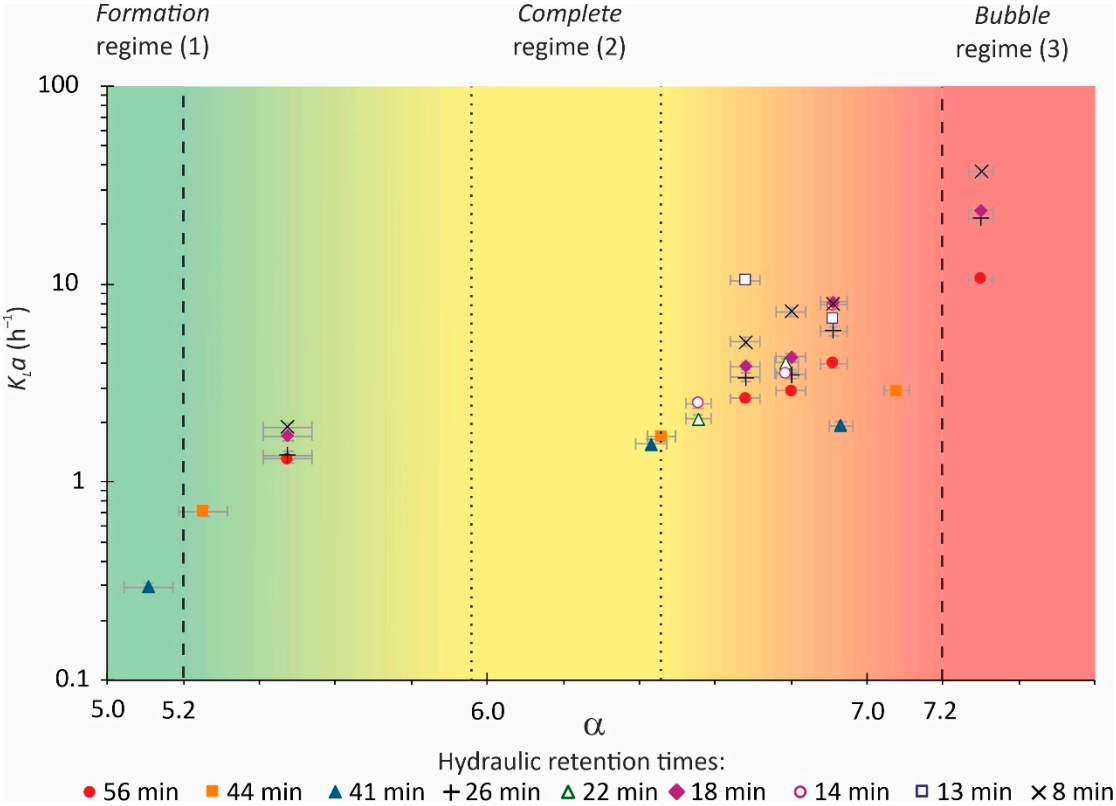

Figure 8. K_La for different α values at different hydraulic retention times. The dashed lines indicate regime transitions; the dotted lines show the intra-regime transitions within the complete regime.

The K_La values inside the bubble regime were rather high compared to, e.g., K_La values of commercially available fine bubble aerators (1.64 h^{-1} [34]) or cascade aerators (4.86 h^{-1} [35]). Inside the bubble regime, high oxygen transfer rates were obtained for HRTs of 8, 18, 41 and 56 min; thus, already short HRTs (8 min) resulted in high K_La values. It should be mentioned that the choice of the design of both impeller and tank (and therefore the α) must be taken into account when designing a system for reaching high DO concentrations, or if one intends to aerate a large quantity of liquid in a short time thus requiring a high K_La. An ideal aeration system should be able to provide both. The obtained data indicated that the impeller system investigated was capable of doing so in the bubble region.

For small α values, the DO_{eq} concentration and the K_La were low and therefore, it could be concluded that, in the formation regime, the aeration capabilities of the system were moderate. This was mainly due to the small interface area created by the relatively low rotation in a given tank geometry.

Most of the experiments in this work were performed in the complete regime. The interface area varied considerably for a given geometry, when the rotational speed was increased. It was noted that, of all three regimes, the complete regime showed the most

significant changes in surface area inside its own region, thus presenting a wide range of equilibrium DO concentrations (1.94–7.09 mg L^{-1}) and K_La (0.71–10.45 h^{-1}). The HRT also influenced the DO_{eq} and, in the complete regime region as shown in Figure 5, it was clearly visible that for higher HRTs (56 min) the DO concentration was higher, too. This was due to the longer aeration period. The longer the water stayed in the tank, the more oxygen was transferred from the air to the liquid mass.

The presence of bubbles in the system suggested an increase in the aeration capabilities, mainly due to the rise in surface area created, thus, in the bubble regime, high DO concentrations (8.45–9.13 mg L^{-1}) and K_La values (10.56–37.09 h^{-1}) were achieved.

3.4. Relation between Interfacial Area and K_La

In order to better understand the relationship between interfacial area and aeration in the system investigated, we tested if K_L was constant with respect to α by dividing the data in Figure 8 by the fit in Figure 6. The results can be seen in Figure 9, separated by regimes including the best fit average K_L. Within the formation and complete regimes, a Pearson-R test showed no significant ($p < 0.87$ for the formation and $p < 0.16$ for the complete regime) correlation with α, so we considered K_L to be a constant within these regimes. However, since the spread of K_L between experiments was quite large, the actual diffusion rate likely depended on specific turbulent conditions in the boundary layer flow. The bubble regime did not allow a statistical analysis, as it was not possible to determine the real interfacial area created by the bubbles.

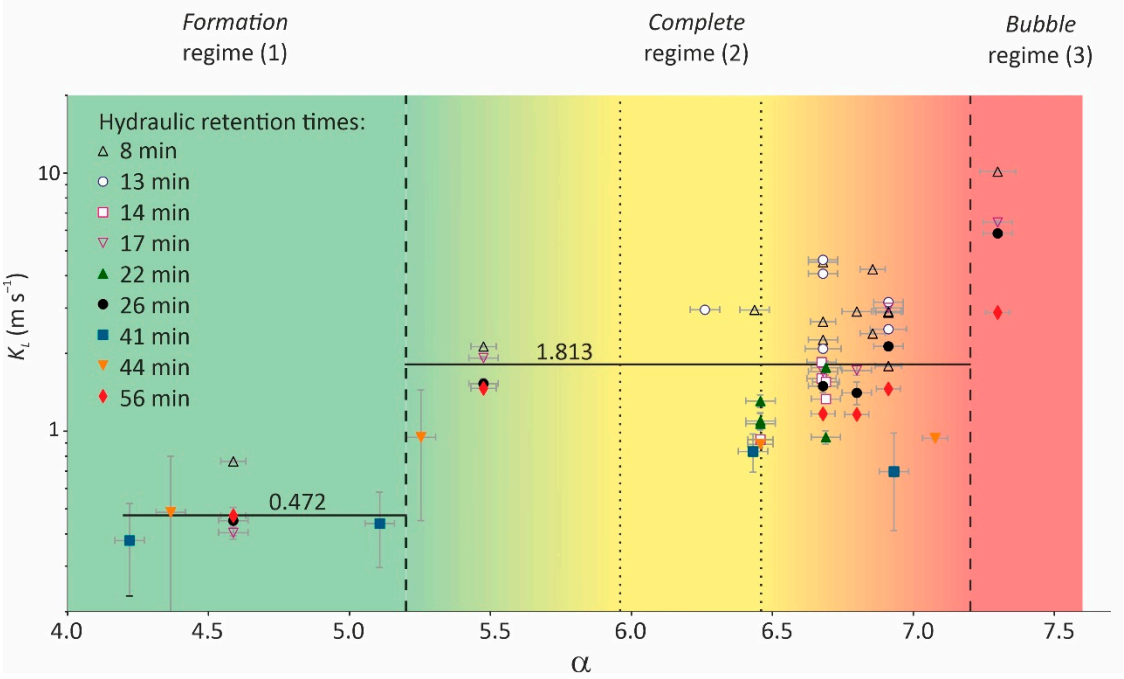

Figure 9. K_L as a function of α for the three regimes. Since the interfacial area in the bubble regime could not be measured directly, the shown values are based solely on the central surface dip. The dashed lines indicate regime transitions; the dotted lines show the intra-regime transitions within the complete regime.

3.5. Redox Potential

Redox potential, or oxidation reduction potential (ORP), is a measure of the tendency of a chemical species to acquire or lose electrons and thereby be reduced or oxidized, respectively [36]. Many factors can influence ORP changes and the kinetics of iron oxidation. The most important are hydrogen sulfide (which was below the limit of detection for the water treated in this work, see Table 2) as well as CO_2 [37]. Usually, ORP is also related to dissolved oxygen—that is, the higher the DO concentration in water, the higher the

redox potential. Redox potentials measured for different experimental configurations are presented in Figure 10.

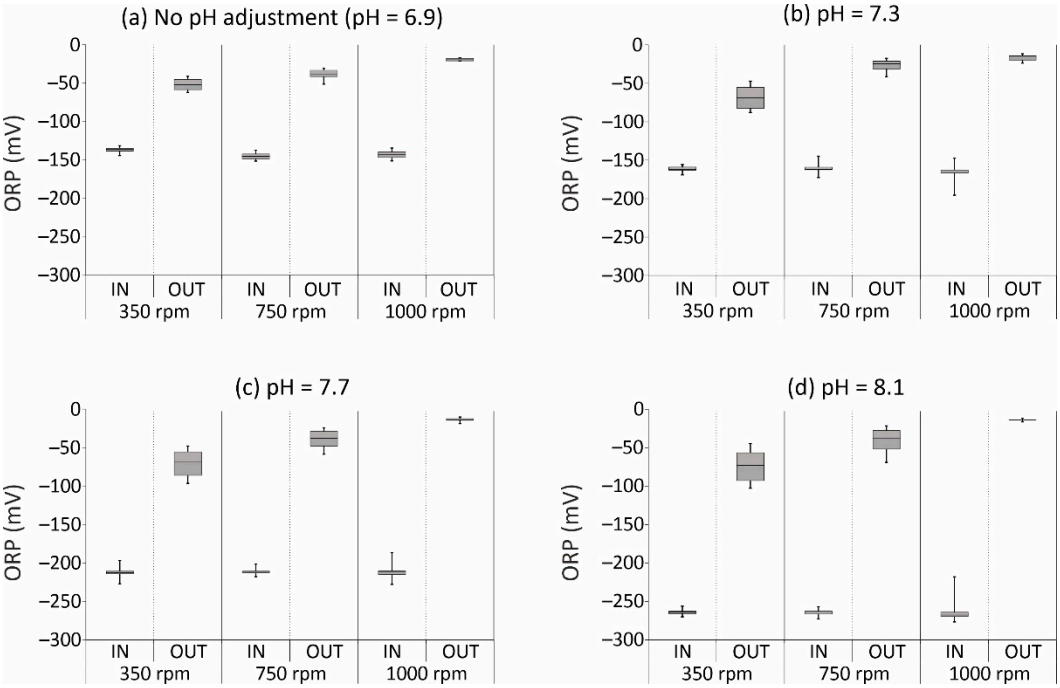

Figure 10. Redox potentials at inlet and outlet for various rotation rates at 0.38 L min^{-1} and 30 cm water column height (HRT = 55 min): (**a**) without NaOH dosing at a pH of 6.91; (**b**) with NaOH dosing at pH 7.3; (**c**) at a higher NaOH dosing at pH 7.7; (**d**) at the highest pH dosing at pH 8.1.

In all the experiments, the redox potentials in both the inlet and outlet were negative with more negative values at the inlet. The reason for that was the high tendency of the Fe^{2+} to lose electrons, i.e., to be oxidized. After the aeration process, the redox potential increased because of the higher DO concentration and lower concentration of Fe^{2+}.

The relation between pH and the inlet redox potential can be given by the well-known Nernst equation,

$$E = E_0 + \left(\frac{RT}{zF}\right) \ln\left\{\frac{a_{red}}{a_{ox}}\right\} \quad (11)$$

where E is the redox potential, E_0 is the standard potential at 25 °C, R is the general gas constant, T the absolute temperature in K, z the number of electrons transferred, F the Faraday constant, and a are the activities of the species involved. From this equation, a direct proportionality of the ORP and the pH can be deduced,

$$E \sim -0.059V \cdot \text{pH} \quad (12)$$

The higher the pH, the lower is the inlet ORP. This can be explained by the increase in OH^- in the water and a higher availability of species to oxidize Fe^{2+}. Additionally, it was noted that. for higher rotation rates and pH levels, the outlet ORP was higher, due to the high oxygen concentration and lower Fe^{2+} concentration after aeration.

3.6. Iron Oxidation

Figure 11 presents the Fe^{2+} oxidation efficiency for different α values in different pH conditions. At higher α values, more DO was available to oxidize Fe^{2+}, thus there was more iron oxidation. The Fe^{2+} concentration in the inlet varied from 4.56 to 5.65 mg L^{-1} and the outlet concentration varied from 0.8 to 3.92 mg L^{-1}.

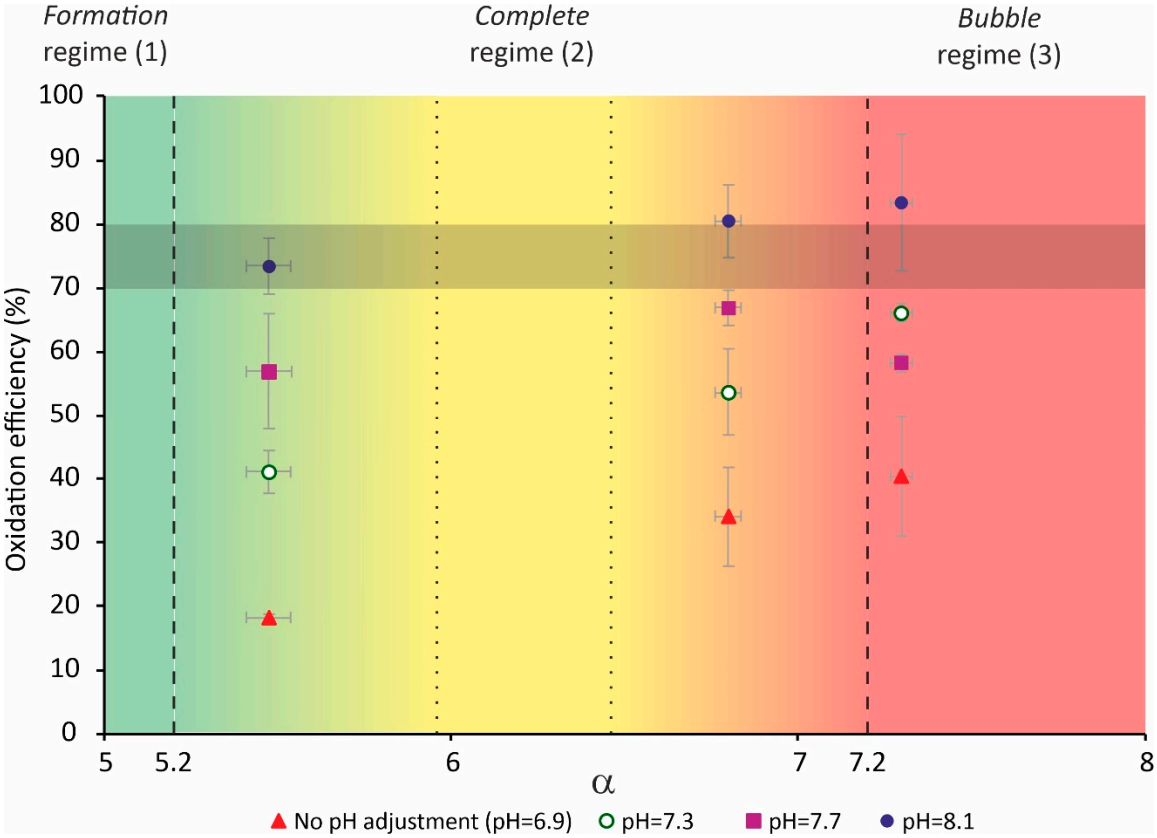

Figure 11. Iron oxidation for different α in different pH conditions. The darkened area shows representative oxidation efficiencies reported by Sharma [7]. The dashed lines indicate regime transitions; the dotted lines show the intra-regime transitions within the complete regime.

Generally, there was no prominent increase in iron oxidation when transitioning from the complete regime to the bubble regime (at pH 7.7 there was a small decrease, but when taking the error bars of the efficiency in the formation regime into account, the changes at this pH were not significant). Thus, when a certain DO concentration was reached, an additional increase did not play an important role in Fe^{3+} oxidation, suggesting that DO was no longer the limiting factor of the oxidation.

At higher pH values (7.7 and 8.1), the iron oxidation efficiency increased. The chemical equilibrium in reaction of Equation (3) was shifted to the right, since free hydroxyl ions were available for $Fe(OH)_3$ precipitation or, in the case of pH 8.1, the beginning of the formation of $Fe(OH)_4^-$ [38]. The oxygen concentration was measured only in-line and not in the sample, so it was assumed to be the same. The highest efficiencies (83, 80 and 73%) were obtained with pH = 8.1 and α = 7.3, 6.8 and 5.48, respectively. This means that when O_2 was in excess in the reaction, the pH condition played a more significant role in the process.

4. Conclusions

The vortex impeller system presented in this paper exhibited robust and efficient aeration capability. This capability can best be evaluated using the proposed α coefficient, which permitted a complete analysis of the system, combining different variables such as water height, volume, rotational speed, tank design and impeller design into one dimensionless coefficient.

There was a direct relationship between the interfacial area and oxygen transfer capabilities; for a larger surface area, higher DO_{eq} and K_La values could be achieved. These results showed that the impeller system studied in this work represented an effective and commercially competitive aeration technology. The vortex impeller system also provided

interesting results for Fe^{2+} oxidation in groundwater. At a high DO concentration and a high pH, the iron oxidation efficiency of the system increased to 83%. After a certain DO threshold, the oxidation rates could be further increased by increasing the pH. Even though more experiments must be conducted to determine energy-related coefficients, the performance observed indicated that the presented vortex impeller flow-through aeration system was applicable for aeration and iron oxidation in ground water due to the large water–air interface created and its high mechanical mixing capability. The dimensionless parameter α could provide engineers with the possibility to scale it according to their desired water volume and flow.

Author Contributions: Conceptualization, M.V.v.d.G., L.L.F.A., E.C.F. and W.L.; data curation, M.v.d.A., L.L.F.A., F.W., M.V.v.d.G. and Y.S.; formal analysis, M.V.v.d.G. and L.L.F.A.; investigation, M.V.v.d.G. and L.L.F.A.; methodology, L.L.F.A. and E.C.F.; project administration, E.C.F., L.L.F.A. and W.L.; resources, L.L.F.A. and E.C.F.; supervision, L.L.F.A., E.C.F. and W.L.; validation, L.L.F.A. and M.V.v.d.G.; visualization, L.L.F.A. and Y.S.; writing—original draft, M.V.v.d.G., M.v.d.A., F.W. and Y.S.; writing—review and editing, E.C.F., L.L.F.A. and W.L. All authors have read and agreed to the published version of the manuscript.

Funding: This research received no external funding.

Data Availability Statement: The data is available from the corresponding author upon request.

Acknowledgments: This work was performed at Wetsus, European Centre of Excellence for Sustainable Water Technology (www.wetsus.eu, accessed on 1 January 2022). Wetsus is co-funded by the Dutch Ministry of Economic Affairs and Ministry of Infrastructure and Environment, the Province of Fryslân, and the Northern Netherlands Provinces. The authors would like to thank the participants of the research theme "Applied Water Physics" for the fruitful discussions.

Conflicts of Interest: The authors declare no conflict of interest.

References

1. Gude, J.C.J.; Rietveld, L.C.; van Halem, D. As(III) oxidation by MnO_2 during groundwater treatment. *Water Res.* **2017**, *111*, 41–51. [CrossRef]
2. Leupin, O.X.; Hug, S.J. Oxidation and removal of arsenic (III) from aerated groundwater by filtration through sand and zero-valent iron. *Water Res.* **2005**, *39*, 1729–1740. [CrossRef]
3. Paul, J.M.; Vijayan, A.M.; Raju, A.; Megha, C.; Sadique, K. Comparison of Iron Removal Effeciency by Areation and Adsorption. *IOSR J. Mech. Civ. Eng. (IOSR-JMCE)* **2016**, *13*, 1–4.
4. Mueller, J.; Boyle, W.C.; Popel, I.H.J. *Aeration Principles and Practice*, 1st ed.; CRC Press LLC: Boca Raton, FL, USA, 2002; Volume 11.
5. Åmand, L.; Olsson, G.; Carlsson, B. Aeration control—A review. *Water Sci. Technol.* **2013**, *67*, 2374–2398. [CrossRef]
6. Rosso, D.; Larson, L.E.; Stenstrom, M.K. Aeration of large-scale municipal wastewater treatment plants: State of the art. *Water Sci. Technol.* **2008**, *57*, 973–978. [CrossRef]
7. Chaturvedi, S.; Dave, P.N. Removal of iron for safe drinking water. *Desalination* **2012**, *303*, 1–11. [CrossRef]
8. Sharma, S. Adsorptive Iron Removal from Groundwater. Ph.D. Thesis, Wageningen University, Wageningen, The Netherlands, 2001.
9. Sharma, S.; Petrusevski, B.; Owore, D.; Schippers, J.C. Optimization of floc formation in iron removal from groundwater. In Proceedings of the Asian Waterqual 2003: IWA Asia-Pacific Regional Conference, Bangkok, Thailand, 20–22 October 2003; pp. 20–22.
10. Krupińska, I. Effect of Organic Substances on the Efficiency of Fe(ii) to Fe(iii) Oxidation and Removal of Iron Compounds from Groundwater in the Sedimentation Process. *Civ. Environ. Eng. Rep.* **2017**, *26*, 15–29. [CrossRef]
11. Marjani, A.; Nazari, A.; Seyyed, M. Alteration of Iron Level in Drinking Water by Aeration in Gonbad Kavoos (North East of Iran). *Am. J. Biochem. Biotechnol.* **2009**, *5*, 94–97. [CrossRef]
12. Siabi, W.K. Aeration and its application in groundwater purification. In Proceedings of the 33rd WEDC International Conference—Acces to Sanitation and Safe Water: Global Partnerships and Local Actions, Acra, Ghana, 7–11 April 2008; pp. 495–499.
13. Vries, D.; Bertelkamp, C.; Schoonenberg Kegel, F.; Hofs, B.; Dusseldorp, J.; Bruins, J.H.; van den Akker, B. Iron and manganese removal: Recent advances in modelling treatment efficiency by rapid sand filtration. *Water Res.* **2017**, *109*, 35–45. [CrossRef]
14. Busciglio, A.; Montante, G.; Kracík, T.; Moucha, T.; Paglianti, A. Rotary sloshing induced by impeller action in unbaffled stirred vessels. *Chem. Eng. J.* **2017**, *317*, 433–443. [CrossRef]
15. Distelhoff, M.F.W.; Marquis, A.J. Scalar mixing in the vicinity of two disk turbines and two pitched blade impellers. *Chem. Eng. Sci.* **2000**, *55*, 1905–1920. [CrossRef]

16. Kumaresan, T.; Joshi, J.B. Effect of impeller design on the flow pattern and mixing in stirred tanks. *Chem. Eng. J.* **2006**, *115*, 173–193. [CrossRef]
17. Prakash, B.; Bhatelia, T.; Wadnerkar, D.; Shah, M.T.; Pareek, V.K.; Utikar, R.P. Vortex shape and gas-liquid hydrodynamics in unbaffled stirred tank. *Can. J. Chem. Eng.* **2019**, *97*, 1913–1920. [CrossRef]
18. Stanbury, P.F.; Whitaker, A.; Hall, S.J. Aeration and agitation. In *Principles of Fermentation Technology*, 3rd ed.; Butterworth-Heinemann: Kidlington, UK, 2016; pp. 537–618.
19. Zheng, Z.; Sun, D.; Li, J.; Zhan, X.; Gao, M. Improving oxygen transfer efficiency by developing a novel energy-saving impeller. *Chem. Eng. Res. Des.* **2018**, *130*, 199–207. [CrossRef]
20. Petříček, R.; Moucha, T.; František, J.R.; Valenz, L.; Haidl, J.; Čmelíková, T. Gas-liquid-solid volumetric mass transfer coefficient and impeller power consumptions for industrial vessel design. *Int. J. Heat Mass Transf.* **2018**, *121*, 653–662. [CrossRef]
21. Baeten, J.E.; van Loosdrecht, M.C.M.; Volcke, E.I.P. When and why do gradients of the gas phase composition and pressure affect liquid-gas transfer? *Water Res.* **2020**, *178*, 115844. [CrossRef]
22. Nienow, A.W.; Wisdom, D.J.; Middleton, J.C. The effect of scale and geometry on flooding, recirculation and power in gassed stirred vessels. In Proceedings of the Second European Conference on Mixing, Cambridge, UK, 30 March–1 April 1977; Volume F1, pp. 1–16.
23. Busciglio, A.; Caputo, G.; Scargiali, F. Free-surface shape in unbaffled stirred vessels: Experimental study via digital image analysis. *Chem. Eng. Sci.* **2013**, *104*, 868–880. [CrossRef]
24. Busciglio, A.; Scargiali, F.; Grisafi, F.; Brucato, A. Oscillation dynamics of free vortex surface in uncovered unbaffled stirred vessels. *Chem. Eng. J.* **2016**, *285*, 447–486. [CrossRef]
25. Mulligan, S. Experimental and Numerical Analysis of Three-Dimensional Free-Surface Turbulent Vortex Flows with Strong Circulation. Ph.D. Thesis, Institute of Technology, Sligo, UK, 2015.
26. Jacobi, J. (H2MOTION b.v., Jagerskade 17b, 3552 TL, Utrecht, The Netherlands). Personal communication. 2018.
27. Hummel, F.C.; Willard, H.H. Determination of Iron in Biological Materials the Use of o-Phenanthroline. *Ind. Eng. Chem. Anal. Ed.* **1938**, *10*, 13–15. [CrossRef]
28. Van Beek, C.G.E.M.; Dusseldorp, J.; Joris, K.; Huysman, K.; Leijssen, H.; Schoonenberg-Kegel, F.; de Vet, W.W.J.M.; van de Wetering, S.; Hofs, B. Contributions of homogeneous, heterogeneous and biological iron(II) oxidation in aeration and rapid sand filtration (RSF) in field sites. *J. Water Supply Res. Technol.-Aqua* **2016**, *65*, 195–207. [CrossRef]
29. Tribe, L.A.; Briens, C.L.; Margaritis, A. Determination of the Volumetric Mass Transfer Coefficient (kLa) Using the Dynamic "Gas Out-Gas In" Method: Analysis of Errors Caused by Dissolved Oxygen Probes. *Biotechnol. Bioeng.* **1995**, *46*, 388–392. [CrossRef]
30. Luo, P.; Wu, J.; Pan, X.; Zhang, Y.; Wu, H. Gas-liquid mass transfer behavior in a surface-aerated vessel stirred by a novel long-short blades agitator. *AIChE J.* **2016**, *62*, 1322–1330. [CrossRef]
31. Torricelli, E. De solido hyperbolico acuto. In *Opera Geometrica Evangelistae Toricellii*; typis A. Masse & L. de Landis: Florence, Italy, 1641.
32. Boggs, P.T.; Rogers, J.E. *Orthogonal Distance Regression, NISTIR 89-4197*; U.S. Department of Commerce, Applied and Computational Mathematics Division, National Institute of Standards and Technology: Gaitherburg, MD, USA, 1989.
33. Mozley, S. Calculating Oxygen Percent Saturation and Comments on Controls of Oxygen Saturation, ZO 419/519 Laboratory Exercises. 2002. Available online: https://projects.ncsu.edu/cals/course/zo419/oxygen.html (accessed on 9 September 2020).
34. Thacker, N.; Katkar, S.; Rudra, A. Evaluation of Mass-Transfer Coefficient of Free Fall—Cascade-Aerator. *Environ. Monit. Assess.* **2002**, *74*, 1–9. [CrossRef]
35. Zhou, X.; Wu, Y.; Shi, H.; Song, Y. Evaluation of oxygen transfer parameters of fine-bubble aeration system in plug flow aeration tank of wastewater treatment plant. *J. Environ. Sci.* **2013**, *25*, 295–301. [CrossRef]
36. Suslow, T.V. Oxidation-Reduction Potential for Water Disinfection Monitoring, Control, and Documentation. *ANR Publ.* **2004**, *8194*, 1–5.
37. O'Sullivan, C.; Clarke, W.; Lockington, D. Sources of Hydrogen Sulfide in Groundwater on Reclaimed Land. *J. Environ. Eng.* **2005**, *131*, 471–477. [CrossRef]
38. Grundl, T.; Delwiche, J. Kinetics of ferric oxyhydroxide precipitation. *J. Contam. Hydrol.* **1993**, *14*, 71–97. [CrossRef]